# Physical insight into interactions of interstitial loops and dislocation lines in austenitic high entropy alloys: atomic-scale modelling

Ayobami Daniel Daramola, Anna Fraczkiewicz, Giovanni Bonny, Gilles Adjanor, Ghiath Monnet, Christophe Domain

Journal of Nuclear Materials 592 (2024) 154959

Contents lists available at ScienceDirect

Journal of Nuclear Materials

journal homepage: www.elsevier.com/locate/jnucmat

# Physical insight into interactions of interstitial loops and dislocation lines in austenitic high entropy alloys: atomic-scale modelling

Ayobami Daramola [a,*], Anna Fraczkiewicz [a], Giovanni Bonny [b], Gilles Adjanor [c], Ghiath Monnet [c], Christophe Domain [c]

[a] MINES Saint-Etienne, Université de Lyon, CNRS, UMR 5307 LGF, Centre SMS, Saint-Etienne 42023, France
[b] SCK CEN, Nuclear Energy and Technology Institute, Boeretang 200, B-2400 Mol, Belgium
[c] Département Matériaux et Mécanique des Composants, EDF Lab, Les Renardières, F-77250 Moret sur Loing, France

## GRAPHICAL ABSTRACT

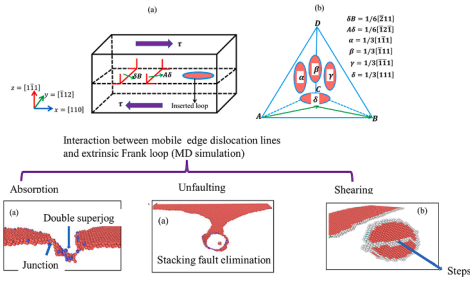


## ARTICLE INFO

*Keywords:*
Radiation hardening
Molecular dynamics
Dislocation
Frank loop
Unfaulting process
Austenitic high entropy alloys
Austenitic stainless steels

## ABSTRACT

Nuclear reactor materials undergo significant changes in their microstructure and mechanical properties due to radiation exposure. Understanding the role of radiation-induced defects in these materials is a complex challenge, especially for new candidate material. This study utilizes molecular dynamics (MD) simulations with a novel interatomic potential to investigate the interactions between mobile edge dislocation lines and interstitial Frank loops within the quaternary model austenitic high entropy alloy (HEA) $Cr_{15}Fe_{46}Mn_{17}Ni_{22}$. This candidate alloy is referenced as "Y3-HEA". The behavior of this alloy is compared to that of a ternary alloy ($Cr_{20}Fe_{70}Ni_{10}$) considered as a model of classical austenitic stainless steel (ASS).

The investigation begins with molecular statics analysis, focusing on the unfaulting process of interstitial Frank loops. A simplified thermodynamic model is introduced to predict the critical size at which a Frank loop can undergo unfaulting. Complementing this, MD simulations explore several variables, including loop orientation, random seed configuration, temperature, loop size, and intersection interactions. Through this examination, interaction mechanisms between mobile edge dislocations and interstitial Frank loops in Y3-HEA are classified and comparisons are drawn with those observed in ASS.

Furthermore, an average obstacle strength parameter is calculated for both ASS and Y3-HEA and its value is integrated into a radiation hardening constitutive model. This approach allows for the prediction of the contribution of dislocation loops to the hardening behavior of the studied alloys.

* Corresponding author.
*E-mail address:* ayobami.daramola@emse.fr (A. Daramola).

https://doi.org/10.1016/j.jnucmat.2024.154959
Received 26 October 2023; Received in revised form 29 January 2024; Accepted 5 February 2024
Available online 6 February 2024

## 1. Introduction

Structural materials employed in nuclear power reactors undergo significant transformations due to neutron irradiation [1–5]. These materials must endure intense radiation exposure, which can reach up to 100 dpa (displacements per atom) during extended operational periods [1,4,5]. Neutron radiation induces the formation of point defects in materials, leading over time to the formation of defect clusters such as linear defects (dislocation loops), planar defects (stacking faults), or volumetric clusters (precipitates, voids, stacking fault tetrahedrons, etc.). These defects can adversely affect the mechanical properties of materials, resulting in increased strength but decreased ductility; features that necessitate a comprehensive evaluation for the safety and reliability of nuclear energy systems [1,4].

The reactor core comprises reactor pressure vessels (RPV) that house the fuel assembly and internal components. These internal structures are constructed with components such as core barrel reinforcement and baffle former plates made from 304 L austenitic stainless steel. Furthermore, the baffle bolts are fashioned from cold-worked 316 L austenitic stainless steel. The components operate under temperatures of up to, locally, approximately 630 K [1,4,5]. Although austenitic stainless steels have proven their suitability for these applications, ongoing efforts are directed towards the discovery of new and improved materials.

Recent research has unveiled the potential of high entropy alloys (HEAs) to offer better properties compared to conventional alloys [6]. Some HEAs exhibit remarkable features, including high solid solution and strain hardening, slowed-down phase transformation kinetics and improved radiation resistance [6–9]. For example, face-centered cubic (FCC) structured HEAs, display unique combinations of strength and ductility, with simultaneous increases in both properties especially at cryogenic temperatures [7]. A highly promising High Entropy Alloy (HEA) is the Cantor alloy, which is an equimolar combination of CoCrFeMnNi [6]. This alloy demonstrates superior resistance to void swelling under irradiation compared to conventional alloys [10]. However, its unsuitability for nuclear applications arises from the generation of the $^{60}$Co radioisotope during neutron irradiation. Consequently, research efforts have been directed towards the development of Cobalt-free alloys capable of reproducing the exceptional properties of the Cantor alloy [11–15].

In a study by [14], the $Cr_{18}Fe_{27}Mn_{27}Ni_{28}$ (*at%*) with a single-phase FCC structure had a tensile strength increasing as the test temperature decreased, mirroring the behavior observed in the equimolar CoCrFeMnNi alloy. The authors also noted twinning during deformation at temperatures below 77 K. Further investigations by Kumar et al. [11] involved subjecting the $Cr_{18}Fe_{27}Mn_{27}Ni_{28}$ (*at%*) alloy to $Ni^{2+}$ ion irradiation, revealing mechanical properties similar to those of common austenitic steels made of CrFeNi or CrFeMn alloys. Additionally, the authors demonstrated reduced radiation damage at high temperatures (773 *K*) compared to austenitic steels. Li et al. [15] delved into the impact of neutron irradiation on the same alloy, finding that its diffusion rate was slower compared to conventional FCC alloys. Parkin et al. [12] showcased the promising strength of the $Cr_{18}Fe_{27}Mn_{27}Ni_{28}$ and $Cr_{15}Fe_{35}Mn_{15}Ni_{35}$ alloys in tensile deformation, with yield strengths of 155 *MPa* and 151 *MPa*, respectively, at room temperature; these values gradually decrease to 93 *MPa* and 100 *MPa*, respectively, at 773 *K*.

Recently, Olszewska [16] developed a Co-free alloy, $Cr_{15}Fe_{46}Mn_{17}Ni_{22}$ (*at%*), referred later on as Y3-HEA, exhibiting enhanced FCC structural stability down to 773 K, akin to the Cantor alloy. This alloy also displayed strain hardening characteristics, allowing for substantial increases in yield strength without compromising ductility.

Gao et al. [13] conducted a comprehensive study on the behavior of irradiation-induced dislocation loops in Y3-HEA exposed to various irradiation temperatures. The authors observed that loop densities remained relatively constant, hovering around $5.0 \times 10^{22}$ $m^{-3}$ from 95 *K* to 623 *K* but decreased to approximately $1.05 \times 10^{21}$ $m^{-3}$ at 823 K. The authors concluded that Y3-HEA exhibited loop behavior similar to conventional ternary CrFeNi alloys. Furthermore, the prevailing defect types in Y3-HEA after being subjected to high-dose Fe2+ ion irradiation consisted of faulted Frank loops characterized by a Burgers vector of $1/3\langle 111\rangle$ in the {111} planes, and perfect loops characterized by a Burgers vector of $1/2\langle 110\rangle$ in the {110} planes. These defect types closely resemble those observed in irradiated model austenitic stainless steel [17]. [13] noted that, in Y3-HEA, the fraction of perfect loops exceeded that of Frank loops at irradiation temperature 823 *K*.

As to the type of defects present in irradiated austenitic stainless steel, Chen et al. [17] posited that Frank loops $1/3[111]$ transform into perfect loops $1/2[110]$ at temperatures above 623 *K* with Ni ion irradiation, though no critical loop size was empirically determined. However, the resolution limitations of transmission electron microscopy (TEM) tools continue to pose challenges for researchers seeking an in-depth analysis of loop evolution and reactions.

To complement experimental endeavors, several researchers have employed atomistic modeling to gain insights into loop behavior at the nanoscale. For instance, Chen et al. [18] merged atomistic simulation with a continuum model to predict the existence of a critical loop size for a vacancy Frank loop in pure Al and Ni. Kadoyoshi et al. [19] harnessed molecular dynamics (MD) techniques to explore the formation of stacking fault tetrahedra and the phenomenon of unfaulting of Frank loops in FCC metals, demonstrating that unfaulting processes occur when Frank loops interact with Shockley partial dislocations. Various studies have elucidated unfaulting mechanisms by investigating the interactions between Frank loops and edge or screw dislocations, considering variables such as temperature, loop orientation and random seed distribution [20–25]. Nevertheless, the interaction mechanism between mobile dislocations and dislocation loops in different materials remains a topic of ongoing debate due to the complex nature of these interactions despite their substantial influence on microstructure evolution and radiation-induced hardening on materials.

This study endeavors to delve into the impact of interactions between interstitial Frank loops and a mobile edge dislocation on the mechanical behavior of Y3-HEA, leveraging a newly developed empirical interatomic potential for the CrFeMnNi system [26]. This work approach comprises three key components:

I. Utilizing a thermodynamic and continuum model to forecast the critical loop size at which a Frank loop may unfault, transforming into a perfect loop.
II. Investigating various interaction mechanisms and their associated obstacle strengths under diverse conditions, including temperature, loop orientation, random seed distribution and loop size.
III. Calculating the average obstacle strength parameter for the radiation hardening constitutive model to predict the contribution of dislocation loop hardening to overall radiation hardening.

The simulation outcomes for Y3-HEA are compared to those obtained in similar conditions for a model austenitic stainless steel (ternary $Cr_{20}Fe_{70}Ni_{10}$ alloy).

## 2. Methods

### 2.1. Simulation techniques

#### 2.1.1. Interatomic potential

The interatomic potential for Cr-Fe-Mn-Ni system employed in this study was developed in our previous work [26] using the embedded atom method (EAM). This potential was derived from the CrFeNi potential by Bonny et al. [27,28]. The accuracy of this potential has been demonstrated in a previous work [29] and the fitting of the potential was

done with experimental and density functional theory (DFT) data, namely the elastic constants of the FCC structure and the stacking fault energy ($\gamma_{SFE}$). The Y3-HEA exhibits phase stability, maintaining an FCC phase across all studied temperatures, as determined by the interatomic potential. This was confirmed by ensuring a positive cohesive energy difference between FCC and BCC (body centered cubic) phases. Additionally, assessments of the tetragonal shear modulus (C′), a crucial indicator for phase stability during deformation, were conducted. The interatomic potential predicts C′ within the 54 *GPa* range for Y3-HEA, affirming the stability of the FCC phase under small elastic deformation. This aligns with expectations for concentrated alloys, as the tetragonal shear modulus (C′) is anticipated to exceed 10 *GPa*, as highlighted by Bonny et al. [27]. Further details on the predicted phase stability of the CrFeMnNi system using the interatomic potential are available in Daramola et al. [26].

### 2.1.2. Construction of edge dislocation and Frank loop

The generation of the glissile edge dislocation employed Bacon's method [30]. Dislocation's dissociation was taken into account, in agreement with the calculated SFE of the structure. The simulation box, illustrated in Fig. 1a, has dimensions of 42 × 36 × 20$nm^3$ and incorporates approximately 2.59 million mobile chemically random atoms. The atoms are representing the Cr-Fe-Mn-Ni elements for Y3-HEA and Cr-Fe-Ni elements for ASS. The Cartesian coordinate system's the [110],[$\bar{1}$12] and [1$\bar{1}$1] directions correspond to the *x, y* and *z* axes, respectively. Periodic boundary conditions were applied to the x and y axes, while the upper and lower (1$\bar{1}$1) atomic planes were rigidly fixed in position. External loading was induced by shifting the upper fixed (1$\bar{1}$1) atomic planes of the model crystal at a shear rate $(\Delta\dot{\gamma})$ of $10^7$ $s^{-1}$, corresponding to a dislocation velocity of approximately 25 *m/s*. The simulation box's dislocation density value is 1.25 × $10^{15}$ $m^{-2}$. After each shift of the upper fixed layers, the total shear stress $\tau$ $(\pm\tau = F_x/A_{xy})$ corresponding to the applied strain was computed. Here, $F_x$ represents the force magnitude in the x-direction originating from the central and upper region, and $A_{xy}$ denotes the area of the *x-y* plane of the box.

In this study, the interstitial Frank loop assumes an initial circular shape. Three distinct diameters of loop were studied: 2, 5 and 10 *nm*, corresponding to 61, 367 and 1417 self-interstitial atoms (SIA), Table 1. The loop is centered within the simulation box and positioned sufficiently far from the constructed edge dislocation (10 *nm* away from the leading partial dislocation) to ensure that no immediate reactions occur upon system relaxation. Fig. 1b shows the Thompson tetrahedron concept with a Burgers vector of 1/3[111], 1/3[$\bar{1}$11], 1 /3[1$\bar{1}$1] and 1 / 3[$\bar{1}\bar{1}$1] to assign the habit plane (111).

To simulate the system's behavior, Molecular Dynamics (MD) simulations were conducted at various temperatures (ranging from 10 to 900 *K*) using a time step of 1 femtosecond (fs). Initially, velocities were assigned to all atoms following a Maxwell-Boltzmann distribution [31] with an initial temperature (T). The NVT ensemble was employed to maintain the system's N (number of atoms), V (volume) and T (temperature) constants, while thermalizing it. The simulations were executed using the Large-scale Atomic/Molecular Massive Parallel Simulator (LAMMPS) developed by Sandia National Laboratories for parallel computers [32] and the resulting data were visualized using the dislocation extraction algorithm (DXA) [33,34]. Each interaction was computed for three random alloying initial distribution configurations (called "seeds" later) to account for the influence of chemical complexity in concentrated alloys, unlike pure metals.

To ascertain the critical stress and obstacle strength required for the loop to unpin from the dislocations, the friction stress ($\tau_f$) or intrinsic resistance stress plays a pivotal role. Table 2 presents the evaluation of the shear modulus (μ) and friction stress as function of temperature. These values were obtained under defect-free conditions in the simulation box. The methods used to collect all the data in Table 2 can be referenced in Daramola et al. [29].

**Table 1**
The Burgers vector of the Frank loops orientations, the Shockley partial and loop sizes used in this work.

| Loop size (nm) | Number of Self-interstitial atoms (SIA) | Frank loop Burgers vector | | Shockley partial | |
|---|---|---|---|---|---|
| 2 | 61 | $\alpha$ | 1/3[1$\bar{1}$1] | Leading partial $\overrightarrow{A\delta}$ | Trailing partial $\overrightarrow{\delta B}$ |
| 5 | 367 | $\beta$ | 1/3[$\bar{1}$11] | 1/6[$\bar{1}$2$\bar{1}$] | 1/6[$\bar{2}$11] |
| 10 | 1417 | $\gamma$ | 1/3[$\bar{1}\bar{1}$1] | | |
| | | $\delta$ | 1/3[111] | | |

## 3. Results

### 3.1. Loop stability: Frank loop versus perfect loop

The assessment of dislocation loop stability involved the computation of the loop formation energy ($E_{loop}^{form}$) at zero Kelvin (*K*). A Burgers vector of 1/3[111] with a (111) habit plane was introduced for the faulted Frank loops, while a Burgers vector of 1/2[110] with a (110) plane was used for the perfect loop. Eq. (1) was employed to calculate

**Table 2**
The characteristics of dislocation movement in defect-free ASS and Y3-HEA. The Hill approximation is used to calculate the effective isotropic shear modulus value (average of Voigt and Reuss estimation [29].

| Temperature (K) | Calculation with EAM interatomic potential [29] | | | |
|---|---|---|---|---|
| | $\tau_f$ (ASS) (MPa) | $\tau_f$ (Y3) (MPa) | $\mu$ (ASS) (GPa) | $\mu$ (Y3) (GPa) |
| 10 | 376 | 459 | 85 | 90 |
| 300 | 143 | 234 | 80 | 83 |
| 600 | 73 | 147 | 77 | 82 |
| 900 | 48 | 85 | 75 | 80 |

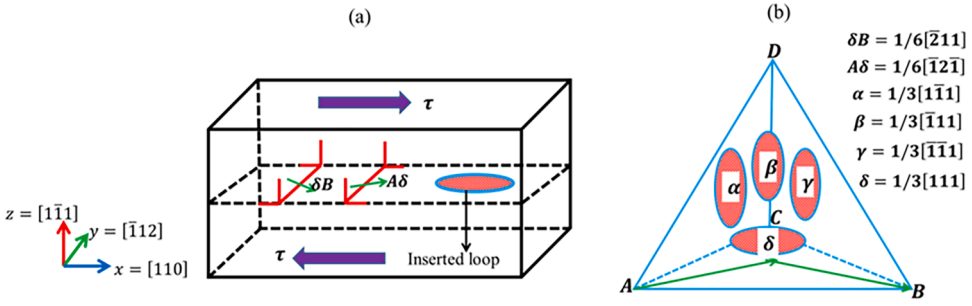


**Fig. 1.** (a) Schematic representation of the simulation cell with a faulted Frank loop (FL) and the edge dislocations. (b) Configurations based on Thompson tetrahedron notations that are used to represent the loop orientation. The different FL with habit planes {111} are denoted with the Greek letters *α*, *β*, *γ* and *δ*.

the formation energy of a loop:

$$E_{loop}^{form} = E(X+N) - \frac{X+N}{X}E(X) \quad (1)$$

where $X$ denotes the total number of atoms in the perfect lattice box, $N$ represents the number of self-interstitial atoms (SIA), $E(X+N)$ signifies the energy of the system with the interstitial atoms (as illustrated in Fig. 2b) and $E(X)$ corresponds to the energy of the system without the interstitial atoms (as illustrated in Fig. 2a). The calculations were iterated 10 times to incorporate a statistical measure, considering the impact of chemical randomness.

On the other hand, the formation energy of a loop, as derived from molecular statics can also serve to fit it into a continuum model based on elastic theory [35]. Thus, ($E_{loop}^{form}$) of a dislocation loop is described by Eq. (2):

$$E_{loop}^{form} = \pi R^2 \gamma_{SFE} + 2\pi f R \bar{K} \ln\left(\frac{R}{r_0}\right) \quad (2)$$

where $\bar{K}$ represents an elastic coefficient dependent on bulk elastic constants, Poisson's ratio and the Burgers vector of the loop. Additionally, $f$ denotes adjustable fitting parameter that ranges from 0 to 1 [35], $r_0$ is the inner cut-off radius, $R$ signifies the radius of the loop, and $\gamma_{SFE}$ is the computed stacking fault energy value using the EAM potential [26].

The configuration of dislocation loops resulting from relaxation through molecular statics calculations for loop formation energy is illustrated in Fig. 3. In Fig. 3, the red atoms represent stacking fault atoms within the hcp structure, while the white atoms correspond to an unknown structure.

Following system relaxation, we observed that the size of the loop influences the shape of the loop. For both Frank and perfect loops with a 2 *nm* diameter (as shown in Fig. 3a and c), we noted that the loop's shape deviated from perfect circularity. This behavior is attributed to the local strain field induced by interstitial atoms, consistent with the explanation proposed by Hayakawa et al. [36] for FCC metals.

However, for both alloys and both types of loops with larger diameters (5 *nm* and 10 *nm*), the circular shape remained intact after relaxation, as demonstrated for the 10 *nm* loops in Fig. 3b and d. This phenomenon can be attributed to isotropic elasticity, in line with the concept posited by Dang et al. [37]. Importantly, the observation of circular Frank and perfect loops with larger diameters aligns with experimental findings in ion-irradiated FCC alloys, as reported by Desormeaux et al., [38] and Xiu et al., [39].

It is important to emphasize that, depending on the irradiation temperature (e.g., 823 *K*), dislocation loops typically observed in Y3-HEA, as documented by Gao et al. [13], tend to have diameters larger than 2 *nm* and exhibit a circular shape, consistent with our findings. However, the limitations of experimental resolution make it challenging to discern smaller loops, such as those with a 2 *nm* diameter. Consequently, it remains uncertain whether these smaller loops also maintain a circular shape. Gao et al., [13] noted the observation of very small loops in Y3-HEA at temperatures $\leq$ 623 *K*.

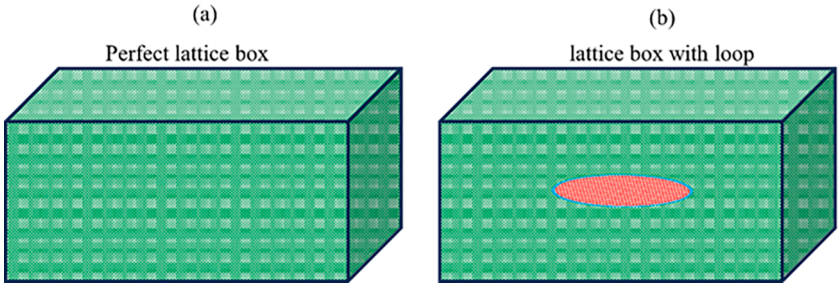


**Fig. 2.** Schematic representation of simulation cell with a) perfect FCC crystal lattice b) an interstitial circular dislocation loop. The [110], [$\bar{1}$12] and [1$\bar{1}$1] directions of the Cartesian coordinate system correspond to the x, y and z axes. No Shockley partial dislocation is present in the box. A Burgers vector of 1 /3[111] with a (111) habit plane was introduced for the faulted Frank loops, while a Burgers vector of 1/2[110] with a ($\bar{1}$10) plane was used for the perfect loop. The green color in the box indicates the FCC bulk material and the red color inside the dislocation loop signifies the stacking fault associated with the loop.

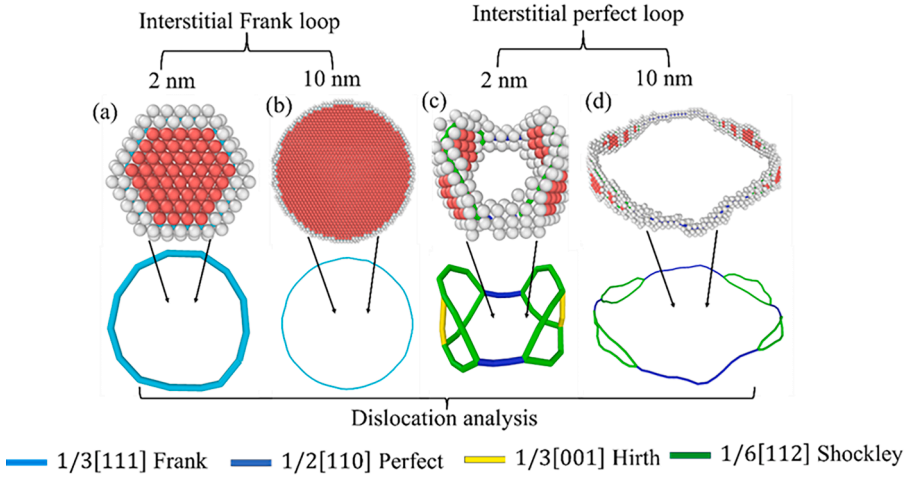


**Fig. 3.** Dislocation loops configurations observed after relaxation. Molecular statics calculation for loop formation energy, case of Y3-HEA alloy. (a) Frank loop of 2 nm; (b) Frank loop of 10 nm; (c) perfect loop of 2 nm and d) perfect loop of 10 nm. The loops were visualized and analyzed using OVITO software [33,34]. Red atoms are stacking fault atoms in hcp structure, while white atoms are present on the dislocation loop line with an unknown structure representation. Dislocation with cyan color is identified as 1/3[111] Frank dislocation, dislocation with blue color is a 1/2[110] perfect dislocation, dislocation with green color is a 1 /6[112] Shockley partial and dislocation with yellow color is a 1/3[001] Hirth lock.

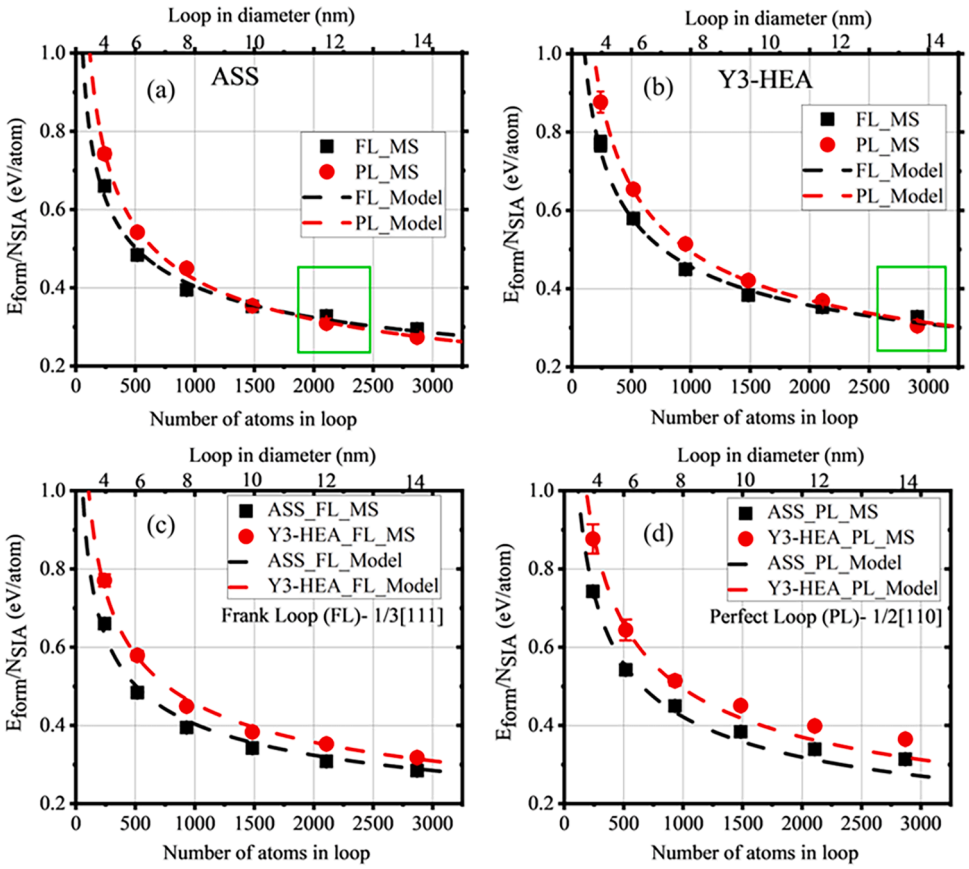


**Fig. 4.** Formation energy of a Frank (FL) and perfect loop (PL) with a Burgers vector of 1/3[111] and 1/2[110] respectively, as a function of their diameter size (2R). Calculation by MS method (points) and the continuum model (dashed lines) using the fitting parameters in Table 3. The green box indicates the point of Frank loop formation energy surpasses perfect loop formation energy. (a) ASS, (b) Y3-HEA (c) Formation energies of Frank loops (FL) in both ASS and Y3-HEA alloys. (d) Formation energies of perfect loops (PL) in both ASS and Y3-HEA alloys. The formation energy calculations were performed for loop sizes ranging from 2 nm to 14 nm.

Fig. 4 illustrates the formation energies of Frank (FL) and perfect loops (PL) with Burgers vectors of1/3[111] and 1/2[110], respectively, in both ASS and Y3-HEA. It is evident that as the number of self-interstitial atoms (SIA) increases, the loop formation energy per atom decreases. These atomistic simulation results have been fitted with a continuum model, and the corresponding parameters used for the fitting are provided in Table 3.

It's worth noting that the model used for this fitting has demonstrated accuracy in previous studies [40] related to loop formation energy in FCC metals. Additionally, Christiaen et al., [41] conducted a comprehensive study involving a combination of Density Functional Theory (DFT), empirical potential, and continuum models, further validating the effectiveness of this approach in predicting structural transitions.

In Fig. 4a and b, a striking trend in loop size is evident. Initially, for smaller loops, Frank Loops (FL) display higher stability, resulting in lower formation energies compared to perfect loops (PL). However, as the loop size increases, this trend reverses, with perfect loops (PL) becoming more stable and consistently exhibiting decreased formation energies.

In Fig. 4c and d, it is evident that the formation energies for both FL and PL are higher in Y3-HEA compared to ASS. This difference can be attributed to the increased chemical complexity of the atomic structure in Y3-HEA. High entropy alloys (HEAs) are known for their significant lattice distortion, driven by the mismatch in atomic sizes [42]. This lattice distortion imposes higher energetic costs when introducing defects like dislocation loops. In the case of Y3-HEA, the lattice mismatch is more pronounced than in ASS, resulting in the observed higher formation energies for dislocation loops. These findings highlight the significant influence of chemical complexity and lattice distortion on the energetics of dislocation loop formation in concentrated alloys. The variation noted in the elastic model arises from discrepancies in elastic moduli between Y3-HEA and ASS, as previously observed in Daramola et al. [26].

### 3.2. Prediction of the critical loop size

The critical loop size, which marks the transition from a less stable faulted loop (like a Frank loop) to a more stable unfaulted loop, is influenced by factors such as temperature, stress, and intrinsic properties of material [23,43,44]. Prior research [17] has debated the existence of this critical loop size for unfaulting, suggesting that if it does exist, it likely falls within the range of 8–12 *nm* or smaller, with Frank loops larger than this expected to unfault.

To predict the critical loop size, elasticity theory provides a useful framework [45]. It states that when the energy difference between a Frank loop and a perfect loop is greater than zero, the radius of the dislocation loop at this point becomes the critical loop size. The formula for this energy difference is as follows:

$$\Delta E = \pi R^2 \gamma_{SFE} - \frac{R\mu a^2}{24}\left(\frac{2-\nu}{1-\nu}\right)\ln\left(\frac{2R}{r_0}\right) > 0 \quad (3)$$

$\Delta E$ is the difference in energy between the Frank loop containing the stacking fault and the perfect dislocation loop after unfaulting, $\mu$ is the shear modulus, $\nu$ is Poisson's ratio, $a$ is the lattice constant related to the Burgers vector of the loop, $r_0$ is the dislocation core radius, and $R$ is the

**Table 3**
Calculation of the formation energy of the Frank loop and perfect loop; the fitting parameters used in Eq. (2). NA; not applicable. $\bar{K}$ represents an elastic coefficient dependent on bulk elastic constants, Poisson's ratio [35] and the Burgers vector of the loop. $f$ denotes adjustable fitting parameter [35], $r_0$ is the inner cut-off radius and $\gamma_{SFE}$ is the computed stacking fault energy value using the EAM potential [26].

| Parameters | ASS | | Y3-HEA | |
|---|---|---|---|---|
| | Frank loop | Perfect loop | Frank loop | Perfect loop |
| $f$ | 1 | 0.9 | 0.81 | 0.75 |
| $\bar{K}(eV/Å)$ | 0.41 | 0.41 | 0.47 | 0.47 |
| $r_0$ $(nm)$ | 0.15 | 0.1 | 0.1 | 0.1 |
| $\gamma_{SFE}$ $(mJ/m^2)$ | 20 | NA | 26 | NA |

radius of the dislocation loop.

Previous studies have shown that for the unfaulting mechanism to occur in extrinsic interstitial Frank loops, the loop interacts with two Shockley partials to remove the extrinsic fault [23,46,47]. One partial glide below the inserted layer, while the other sweeps above the layer, as described by Eq. (4):

$$\frac{1}{6}[\bar{1}2\bar{1}] + \frac{1}{6}[2\bar{1}\bar{1}] + \frac{1}{3}[111] + \mathrm{SF} \rightarrow \frac{1}{2}[110] \tag{4}$$

A thermodynamic energy balance model can be employed to estimate the critical loop size. Various methods have been reported in the literature [18,19], but a straightforward thermodynamic calculation using an appropriate interatomic potential may suffice. In this study, we consider a critical loop size estimation to be applicable when the difference between the formation energy of the Frank loop ($E_{FL}^{form}$) and the perfect loop ($E_{PL}^{form}$) is precisely zero, denoted as $\Delta E = 0$.

$$\Delta E = E_{FL}^{form} - E_{PL}^{form} > 0 \tag{5}$$

Fig. 5 illustrates that the formation energy of the Frank loop becomes progressively unfavorable for loop sizes exceedingly 12 *nm* (equivalent to 2107 SIA) for ASS and around 14 *nm* (equivalent to 2869 SIA) for Y3-HEA, as denoted by the green box. This suggests that as the size of the Frank loop increases, its stability reduces compared to the perfect loop. This prediction aligns with the proposed loop size range (8–12 *nm*) within which unfaulting may occur in FCC concentrated alloys, as suggested by Chen et al., [17].

In the Y3-HEA case, prior experimental findings [13] have detected extrinsic interstitial Frank loops with varied sizes, depending on the irradiation temperature. The smallest loops, approximately 17 *nm*, were observed in the temperature range of 95 *K* to 623 *K*. While no critical loop size was experimentally determined, our calculations indicated a size of 14 *nm* at 0 *K*, reasonably close to the observed 17 *nm* Frank loop within the 95 to 623 *K* temperature range. This suggests a temperature-dependent growth of the experimentally observed loops. Subsequent Gao et al. [13], demonstrated a substantial increase in Frank loop size with rising temperature, reaching an average size of 63 *nm* at 823 *K*. It's essential to acknowledge that kinetic processes, not considered in the thermodynamic molecular static calculations conducted here, may also contribute to the unfaulting process that may be observed from experiments.

The authors [13] also reported that at the elevated temperature of 823 *K*, a substantial portion of the observed loops exhibited a perfect loop configuration rather than the typical Frank loop structure. This observation suggests that as the temperature increases, the stacking fault energy (SFE) associated with Frank loops also increases, making them less stable and more prone to unfaulting. This phenomenon could explain the higher prevalence of perfect loops compared to Frank loops in Y3-HEA at higher temperature, as noted by Gao et al. [13]. The relationship between temperature and the probability of unfaulting and loop absorption will be further explored in section 3.3.

### 3.3. Mechanisms of interactions between a mobile dislocation and an interstitial Frank loop

Molecular dynamics (MD) simulations were used to study interactions between a mobile edge dislocation and an extrinsic Frank loop under different conditions, such as varying temperatures, loop orientations, random seeds, and loop sizes. This section offers a concise overview of the interaction mechanisms identified in Y3-HEA. A more detailed description, along with accompanying videos illustrating these interactions, is available in section S.1 of the supplementary material. Each video is appropriately labeled based on the corresponding reaction type described in Table 4.

The observed reactions in Y3-HEA are categorized into eleven groups based on their primary mechanisms. While some of these interaction mechanisms have been documented in previous studies involving pure FCC metals [22,23], as well as in Fe–$Ni_{50}$ [48], Fe-$Ni_{10}$-$Cr_{20}$ [20,21], this work also introduces a novel mechanism labelled reaction 1c which is fully described in section S.1.3 in the supplementary document.

Table 4 provides a concise overview of the observed interaction mechanisms, systematically categorized into eleven subgroups based on their primary mechanisms. The subgroups, accompanied by their corresponding labels, are delineated as follows:1a - Full absorption with double superjog, 1b - Superjog on the Shockley partial with half absorption, 1c - Superjog shifting on the Shockley partial, 2a - Formation of a new habit plane with a bridge, 2b – Prismatic loop formation after stacking fault elimination, 2c - Unfaulting on leading and trailing partials, 3a - Surface shearing with a step, 3b - Shearing with a bridge

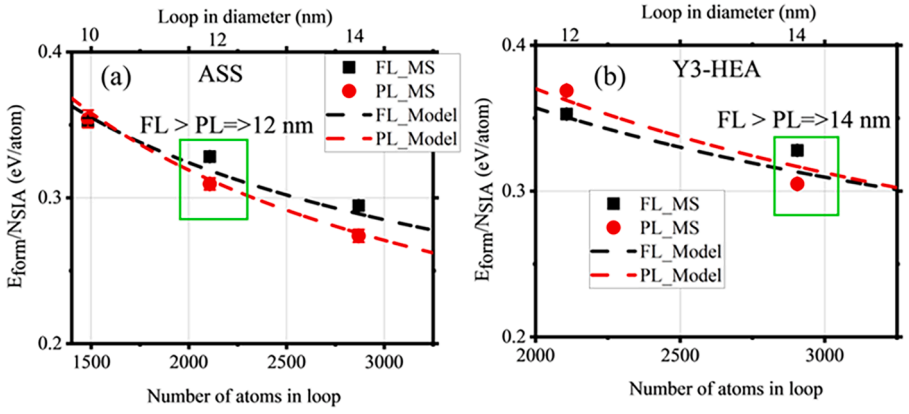


**Fig. 5.** Formation energy of a Frank (FL) and perfect loop (PL) with a Burgers vector of 1/3[111] and 1/2[110] respectively, as a function of their diameter which is 2R. The figure highlights a notable reduction in stability for FL relative to PL, as observed in both (a) ASS and (b) Y3-HEA (zoom-in of Fig. 4).

**Table 4**
Categorization of mobile dislocation-Frank loop interaction mechanisms in MD simulations for Y3-HEA. Summary of all simulation conditions: temperatures 300, 600 and 900 K; loop size 2, 5 and 10 nm; four different loop orientations.

| Interaction mechanism | Label | Description |
|---|---|---|
| Absorption | | |
| | 1a | Absorption into a double "super jog" with constriction. Involves pinning of leading and trailing partials, resulting in the formation of a perfect loop. Vacancy emission observed at lower temperatures. |
| | 1b | Half loop absorption and successive formation of super jog. Involves absorption of the lower half of the loop, formation of a double super jog with a perfect loop shape. |
| | 1c | Formation of super jog with motion on the Shockley partial. Involves pinning of leading partial, formation of super jog, and subsequent shift of super jog along the dislocation line. |
| Unfaulting | | |
| | 2a | Unfaulting with bridge segment and new habit plane. Involves the formation of a bridge connecting trailing partial with upper loop segment, resulting in a new non-coplanar plane. |
| | 2b | Unfaulting with stacking fault removal (prismatic loop). Involves the formation of a D-Shockley partial that eliminates the loop's extrinsic stacking fault. |
| | 2c | Unfaulting occurs when the loop makes contacts with the leading partial and trailing partial. |
| Shearing | | |
| | 3a | Shearing of the loop with step on the surface. Involves loop separation, formation of step vacancies, and nucleation of Shockley partial on the surface. |
| | 3b | Pure shearing with bridge segment before unpinning. Involves formation of a bridge segment before unpinning. |
| | 3c | Pure shearing. Involves loop contact with dislocation line and unpinning with step vacancies on the surface of the loop after interactions |
| | 3d | Shearing with super jog without constriction. Involves bowing deformation of leading partial, formation of a screw dipole, and creation of a super jog. |
| | 3e | Shearing with super jog with constriction. Involves rapid constriction formation, cross slip, and preservation of loop orientation |

**Table 5**
Categorization of mobile dislocation-Frank loop interaction mechanisms in MD simulations for Y3-HEA. Summary of all simulation conditions: temperatures 300, 600 and 900 K; loop size 2 nm (S-Small), 5 nm (M-Medium) and 10 nm (L-Large); four different loop orientations.

| Temperature | | $\alpha = 1/3[1\bar{1}1]$ | $\beta = 1/3[\bar{1}11]$ | $\gamma = 1/3[\bar{1}\bar{1}1]$ | $\delta = 1/3[111]$ |
|---|---|---|---|---|---|
| 10 K | Seed 1 | $3a^{M,L}$, $3c^{S}$ | $3d^{S}$, $3e^{M,L}$ | $3c^{S,M,L}$ | $2c^{S,M,L}$ |
| | Seed 2 | $1b^{S}$, $3a^{M,L}$ | $3d^{S}$, $3e^{M,L}$ | $3b^{S}$, $3c^{M,L}$ | $2c^{S,M,L}$ |
| | Seed 3 | $2a^{S}$, $3a^{M,L}$ | $3d^{S}$, $3e^{M,L}$ | $3e^{S}$, $3c^{M,L}$ | $2c^{S,M,L}$ |
| 300 K | Seed 1 | $3a^{M,L}$, $3c^{S}$ | $3d^{S}$, $3e^{M,L}$ | $3b^{S}$, $3c^{M,L}$ | $2c^{S,M,L}$ |
| | Seed 2 | $1a^{S}$, $3a^{M,L}$ | $2a^{S}$, $3e^{M,L}$ | $3c^{S,M,L}$ | $2b^{M}2c^{S,L}$ |
| | Seed 3 | $1b^{S}$, $3a^{M,L}$ | $3d^{S}$, $3e^{M,L}$ | $3b^{S}$, $3c^{M,L}$ | $3c^{S}$, $2c^{M,L}$ |
| 600 K | Seed 1 | $3a^{M,L}$, $3c^{S}$ | $2a^{S}$, $3e^{M,L}$ | $3c^{S,M,L}$ | $2b^{M}$, $2c^{S,L}$ |
| | Seed 2 | $3a^{M,L}$, $3c^{S}$ | $3e^{S,L}$, $1b^{M}$ | $3b^{S}$, $3c^{M,L}$ | $2c^{S,M,L}$ |
| | Seed 3 | $1a^{S}$, $3a^{M,L}$ | $3d^{S,L}$, $1b^{M}$ | $3b^{S}$, $3c^{M,L}$ | $2c^{S,M,L}$ |
| 900 K | Seed 1 | $1a^{S}$, $3a^{M,L}$ | $3d^{S}$, $3e^{M,L}$ | $3b^{S}$, $3c^{M,L}$ | $3c^{S}$, $2c^{M,L}$ |
| | Seed 2 | $1b^{S}$, $3c^{M}$, $3a^{L}$ | $3a^{S}$, $3e^{M,L}$ | $2a^{S}$, $3c^{M,L}$ | $2c^{S,M,L}$ |
| | Seed 3 | $1a^{S}$, $3a^{M,L}$ | $3d^{S}$, $3e^{M,L}$ | $2a^{S}$, $3c^{M,L}$ | $1c^{S}$, $2c^{M,L}$ |

segment, 3c - Pure shearing, 3d - Cross-slip of screw dislocation dipole with no constriction, 3e - Cross-slip of screw dislocation dipole with constriction.

Additionally, Table 5 offers a comprehensive overview of the complete interaction mechanisms observed across all simulation conditions, with corresponding labels that reference Table 4.

## 4. Discussions

In this discussion, we examine the outcomes of interactions between mobile edge dislocations and extrinsic interstitial Frank loops in Y3-HEA, comparing them to those identified in the ASS model alloy. Both alloys exhibit three primary interaction categories: loop absorption, unfaulting and shearing. These classifications consider various factors such as loop sizes, orientations, temperatures, and random seed distributions, as detailed in Table 5.

However, in the context of Y3-HEA, particularly for loop sizes of 2 nm (referred to as "S"), the primary interaction mechanism identified was loop shearing, accounting for 50% of all observed reaction types across various simulation conditions, as depicted in Fig. 6a. In contrast, for ASS, the predominant and frequently observed interaction mechanism was loop unfaulting, as illustrated in Fig. 6b.

Notably, studies by Hayakawa et al. [43] and Terentyev et al. [48] indicated an increase in shearing mechanisms when the stacking fault energy is low, at the expense of the unfaulting mechanism. Similarly, Lu et al. [49] suggested a decrease in the transformation of faulted Frank loops to unfaulted loops in compositionally complex alloys like Y3-HEA due to lower stacking fault energy.

However, in our study, the stacking fault energy (SFE) of ASS (20 $mJ/m^2$) was lower than that of Y3-HEA (26 $mJ/m^2$). Consequently, one might expect Y3-HEA to exhibit more unfaulting mechanisms than ASS according to Hayakawa et al. [43] and Terentyev et al. [48] suggestion. Surprisingly, this contradicts the results presented in Fig. 6.

A plausible explanation for the lower occurrence of loop unfaulting in Y3-HEA, compared to ASS, during interactions with mobile dislocation lines is that the local stacking fault energy (SFE) fluctuations between the Shockley partials are more pronounced in Y3-HEA than ASS, as shown by Daramola et al. [29]. These significant SFE fluctuations enhance the local lattice friction stress (higher in Y3-HEA than ASS, as indicated in Table 2), hindering the smooth gliding of Shockley partial dislocations necessary for eliminating the stacking fault associated with the Frank loop. Consequently, this suppresses loop unfaulting and absorption in Y3-HEA, aligning with another suggestion of Terentyev et al. [48] that enhanced friction stress suppresses absorption reactions for both edge and screw dislocations.

To validate this explanation, it was observed that, for a 2 nm loop size, the processes of unfaulting and absorption increase with increasing temperature in both alloys. This observation aligns with our proposition that lattice friction stress influences interaction mechanisms. As temperature increases, lattice friction stress decreases due to thermal activation (see Table 2), reducing the impediment of dislocation lines interacting with the Frank loop. Consequently, this increases the

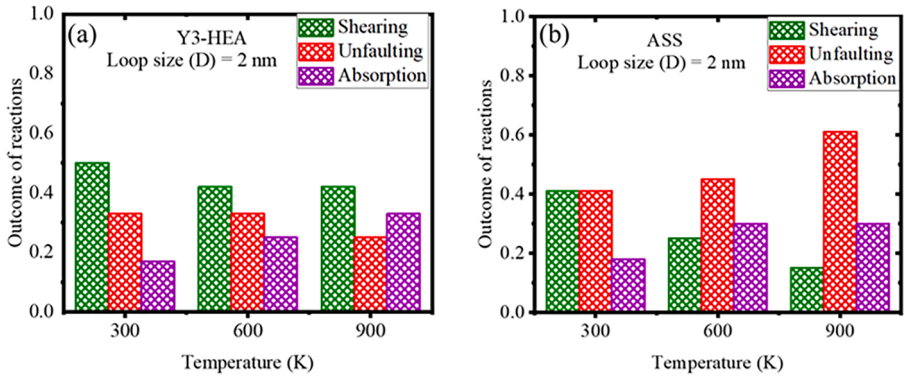


**Fig. 6.** Probability distribution of reaction outcomes at 300 K, 600 K, and for the 2 nm Frank loop in (a) Y3-HEA and (b) ASS.

likelihood of loop unfaulting and absorption, which is also consistent with findings by Nogaret et al. [22]. It is important to note that the impact of random seeds is significant for the reaction mechanism due to the chemical randomness of concentrated alloys.

For sizes of 5 *nm* and 10 *nm*, a loop shearing mechanism was observed in approximately 95% of the total number of configurations. This is in agreement with observations made by Baudouin et al., [20] for classical austenitic stainless steel- $Fe_{70}Ni_{10}Cr_{20}$ alloy (ASS).

### 4.1. Critical stress and obstacle strength analysis

When a dislocation experiences an applied stress $\tau_{app}$ and encounters a point obstacle, it undergoes bowing, and the force exerted by the dislocation on the point defect can be expressed as follows:

$$F = 2\Gamma cos(\varphi) \tag{6}$$

Here, $\Gamma$ represents the line tension of the dislocation and $\varphi$ is the bowing angle. However, defining the line tension in the vicinity of the obstacle becomes challenging due to the complex and strong interaction among the dislocation segments surrounding it. Nonetheless, the line tension can be approximated as $0.5\mu b^2$, where $\mu$ stands for the shear modulus (as shown in Table 2), and $b$ is the magnitude of the Burgers vector.

The force along the dislocation line can be described using the Peach and Koehler force equation:

$$\mathrm{F} = (\tau_{app} - \tau_f)bl \tag{7}$$

where $l$ represents the segment length bowing out into an arc between two obstacles, and $\tau_f$ is the friction stress evaluated without the presence of a Frank loop for the equivalent strain rate (see Table 2).

The maximum applied stress $\tau_{max}$ required for unpinning to occur, allowing the dislocation to continue gliding without interacting with the obstacle, can be given as:

$$\tau_{max} - \tau_f = \frac{\mu b}{l}\cos(\varphi_c) \tag{8}$$

Here, $\varphi_c$ is the critical bowing angle at which the dislocation becomes unpinned. However, determining the angle $\varphi_c$ is challenging because the curvature of the dislocation segments varies significantly in the vicinity of the obstacle. Therefore, Eq. (8) can be reformulated as follows:

$$\Omega = \frac{(\tau_{max} - \tau_f)l}{\mu b} \tag{9}$$

In this equation, $\Omega$ denotes the strength factor of the obstacle, and $l$ is calculated as $l = L_y - D_{DL}$, where $L_y$ represents the dimension of the simulation box along the y-axis, which corresponds to the length of the dislocation line (36 *nm* in the present case, as mentioned in section 2.2.2), and $D_{DL}$ is the diameter of the Frank loop.

The influence of temperature, loop orientation, and random seeds on the unpinning stress required for the dislocation to overcome the Frank loop strength has been investigated. The average critical unpinning stress ($\tau_{max} - \tau_f$) for the three random seeds with loop sizes of 2, 5 and 10 nm in both ASS and Y3-HEA is presented in Table 6.

The unpinning stress ($\tau_{max} - \tau_f$) for the 2 *nm* Frank loop is depicted in Fig. 7, while Fig. 8 illustrates it for the 10 *nm* Frank loop. It's important to note that the impact of temperature on ($\tau_{max} - \tau_f$) value varies with the loop orientations and size of the Frank loops.

For 2 *nm* loops across all temperatures, the $\beta = 1/3[\bar{1}11]$ loop orientation consistently exhibits the highest unpinning stress, while the lowest unpinning stress varies among the loops featuring $\alpha = 1/3[1\bar{1}1]$ and $\delta = 1/3[111]$ loop orientations. A similar trend is observed in the case of ASS. However, for larger loop sizes of 5 *nm* and 10 *nm*, the obstacle stress displays a regular pattern primarily influenced by loop shearing mechanisms.

In both Y3-HEA and ASS, the $\beta = 1/3[\bar{1}11]$ loop orientation consistently shows the highest obstacle stress, whereas the $\gamma = 1/3[\bar{1}\bar{1}1]$ loop orientation exhibits the lowest obstacle stress. It's worth noting that this study did not specifically explore other types of glissile edge dislocation orientation, but Baudouin et al. [20] emphasized the importance of interaction mechanisms involving different glissile edge dislocation orientations. It becomes apparent that the direction in which the edge dislocation moves also plays a role in the unfaulting and absorption processes of Frank loops, particularly at the 2 *nm* size.

Furthermore, regardless of the specific glissile edge dislocation orientation, the predominant mechanism at the 10 *nm* size remains shearing, which aligns with our work. Additionally, the unpinning stress

**Table 6**
Unpinning stress ($\tau_{max} - \tau_f$) in MPa for loop sizes of 2, 5, and 10 *nm* investigated across all simulation conditions in this study. BV-Burgers vector.

| | | Average critical unpinning stress ($\tau_{max} - \tau_f$) in MPa | | | | | |
|---|---|---|---|---|---|---|---|
| | | ASS | | | Y3-HEA | | |
| BV of FLs | FL size | 300 | 600 | 900 | 300 | 600 | 900 |
| $\alpha$ | 2 | 78 | 62 | 69 | 99 | 82 | 76 |
| | 5 | 124 | 97 | 75 | 148 | 127 | 89 |
| | 10 | 204 | 235 | 131 | 249 | 202 | 215 |
| $\beta$ | 2 | 86 | 88 | 66 | 145 | 104 | 95 |
| | 5 | 159 | 132 | 105 | 208 | 149 | 140 |
| | 10 | 339 | 289 | 212 | 376 | 295 | 284 |
| $\gamma$ | 2 | 85 | 79 | 55 | 95 | 63 | 74 |
| | 5 | 79 | 59 | 52 | 92 | 62 | 91 |
| | 10 | 101 | 86 | 114 | 153 | 123 | 121 |
| $\delta$ | 2 | 60 | 78 | 72 | 102 | 62 | 76 |
| | 5 | 131 | 125 | 96 | 184 | 142 | 134 |
| | 10 | 250 | 281 | 206 | 304 | 250 | 263 |

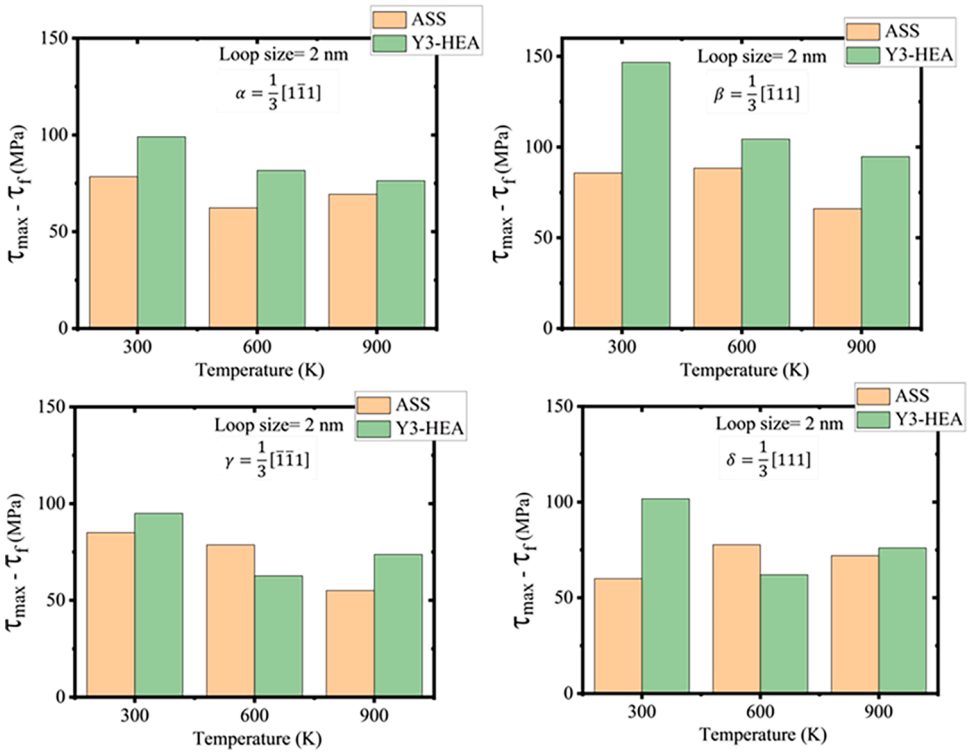


**Fig. 7.** The unpinning stress $(\tau_{max} - \tau_f)$ required for a dislocation to glide through the loop corresponding to different loop orientations and temperature (300–900 K) for a diameter of 2 nm in ASS and Y3-HEA.

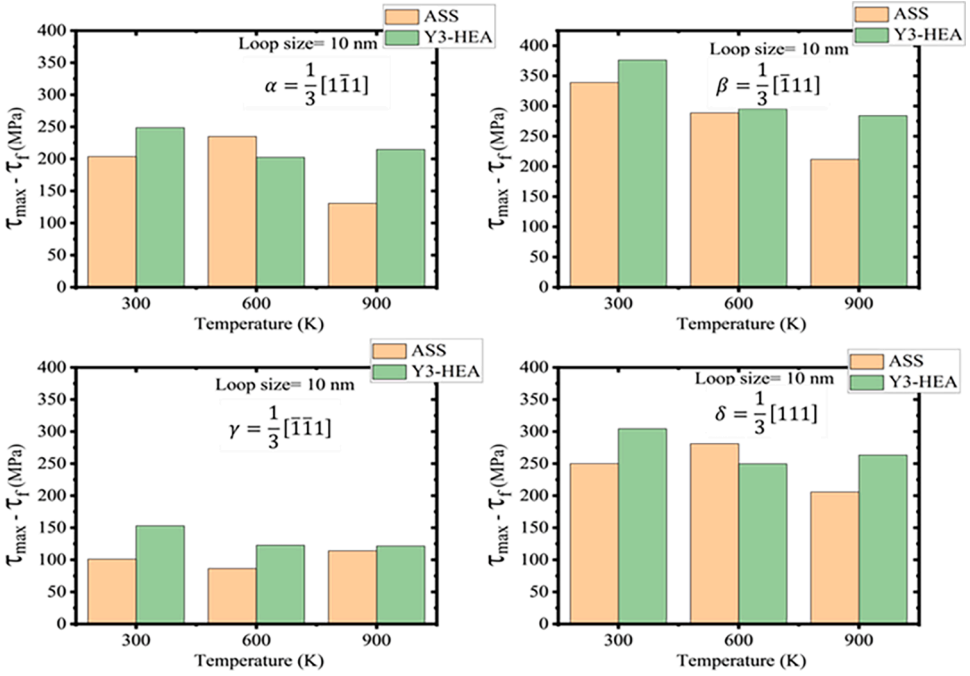


**Fig. 8.** The unpinning stress $(\tau_{max} - \tau_f)$ required for a dislocation to glide through the loop corresponding to different loop orientations and temperature (300–900 K) for a diameter of 10 nm in ASS and Y3-HEA.

$(\tau_{max} - \tau_f)$ decreases with temperature, indicating the presence of thermal activation.

When comparing Y3-HEA and ASS, it's evident that the estimated unpinning stress is higher for Y3-HEA across all simulation conditions. This difference s appears to be influenced by the pronounced friction stress estimated for Y3-HEA.

### *4.2. Analysis and determination of the average obstacle strength parameter for a radiation hardening constitutive model*

To obtain a more accurate estimation of the obstacle strength of a loop, a statistical analysis of interaction of the dislocation with the loop has been done by considering a more realistic situation, in which the

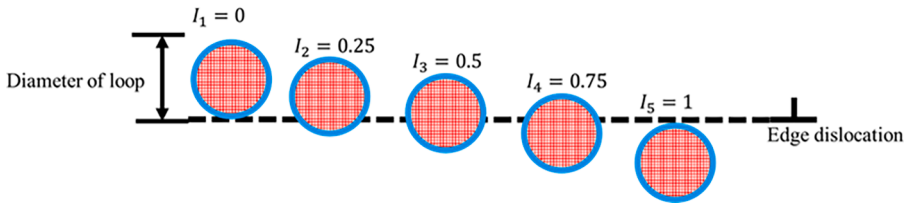


**Fig. 9.** Schematic representation of intersection positions of the edge dislocation and the Frank loop. $I_N$ is the distance between the bottom of the Frank loop and the dislocation glide plane with $I_1 = 0$, $I_2 = 0.25$, $I_3 = 0.5$, $I_4 = 0.75$ and $I_5 = 1$ of loop diameter.

relative position of a loop to a glide plane can be random. Five intersection positions ($I_1$ to $I_5$) were examined (Fig. 9). Simulations were run for each position, except for $I_3 = 0.5$, which was already completed as shown so far. Similar to $I_3 = 0.5$, simulations for $I_1$, $I_2$, $I_4$ and $I_5$ were performed for a 10 nm loop size with three seeds to account for chemical randomness.

The intercept is determined by calculating the ratio of the distance between the dislocation's glide plane and the loop's base plane during interactions, with $I_1 = 0$, $I_2 = 0.25$, $I_3 = 0.5$, $I_4 = 0.75$ and $I_5 = 1$ of loop diameter. The average obstacle strength parameter is then calculated by averaging the obstacles at each intercept ($I$). It is important to note that the specific locations where a dislocation interacts with dislocation loops may significantly affect the interaction mechanisms type observed.

To determine the contribution of small dislocation loops (DL) to radiation hardening, the Monnet's model [50,51], derived from the dispersed barrier hardening model, will be followed. Thus, the average obstacle strength of the loop may be expressed by:

$$\tau_{DL} = \mu b\sqrt{\Omega_{DL} N_{DL} D_{DL}} \tag{10}$$

where $N_{DL}$ is the loop density, $D_{DL}$ is the loop size, μ is the shear modulus, $b$ is the magnitude of Burgers vector and $\Omega_{DL}$ is the strength factor of the dislocation loop which can be obtained using Eq. (9). It's important to note that Eq. (10) is applicable to various types of dislocations, including both perfect and Frank loops, if the distinction between their Burgers vectors is taken into account.

When different dislocations intersect with loops at different heights ($I_N : I_1 - I_5$ in our case), the average obstacle strength barrier leads to DL hardening, as described in Eqs. (11)–(15):

$$\tau_{DL} = \mu b\sqrt{\left\langle \Omega_{DL}^{I_N} \right\rangle_N N_{DL} D_{DL}} \tag{11}$$

$$\tau_{DL} = \sqrt{\left\langle \Omega_{DL}^{I_N} \right\rangle_N}\mu b\sqrt{N_{DL} D_{DL}} \tag{12}$$

$$\bar{\Omega} = \sqrt{\left\langle \Omega_{DL}^{I_N} \right\rangle_N} \tag{13}$$

Using the number of intersection height consider in this work (: $I_1 - I_5$), Eq. (13) becomes:

$$\bar{\Omega} = \sqrt{\frac{\Omega_{DL}^{I_1} + \Omega_{DL}^{I_2} + \Omega_{DL}^{I_3} + \Omega_{DL}^{I_4} + \Omega_{DL}^{I_5}}{5}} \tag{14}$$

where $I$ represent the intersection at different heights and the subscript $N$ is the number of considered intersection heights. By substituting Eq. (14) into Eq. (10), the dislocation loop-induced hardening can be expressed as:

$$\tau_{DL} = \bar{\Omega}_{DL}\mu b\sqrt{N_{DL} D_{DL}} \tag{15}$$

It's worth emphasizing that for each intersection $\Omega_{DL}^{I_N}$ is calculated using Eq. (9) before applying Eq. (14) to obtain an average value.

#### 4.2.1. Influence of temperature on the average obstacle strength parameter

To calculate the average $\bar{\Omega}_{DL}$, we utilized the shear modulus data provided in Table 1 at various temperatures. The resulting $\bar{\Omega}_{DL}$ values are presented in Table 7.

**Table 7**
Average obstacle strength parameter estimation for 10 nm diameter Frank loop at various temperatures using Eq. (14), alongside analytically estimated strength factor for austenitic stainless steel (ASS) at room temperature by Tan and Busby [52].

| Material/ temperature | Average obstacle strength $\bar{\Omega}_{DL}$ (this work) | | | ASS @ room temperature [52] |
|---|---|---|---|---|
| | 300 K | 600 K | 900 K | |
| ASS | 0.57 | 0.56 | 0.53 | 0.47 - 0.54 |
| Y3-HEA | 0.55 | 0.50 | 0.52 | |

In Fig. 10a, the average obstacle strength shows only a slight difference between the two alloys and remains relatively stable across varying temperatures. This trend aligns with Tan & Busby model [52], which estimates the strength factor for different Frank loop sizes. However, Fig. 10b and c emphasize that the maximum stress ($\tau_{max}$) is consistently higher in Y3-HEA when compared to ASS. This disparity can be attributed to the more significant influence of friction stress in Y3-HEA relative to ASS.

Monnet and Devincre [53] argue that friction stress significantly affects the motion of dislocation segments in contact with obstacles, impeding their complete interaction with the loop. Nevertheless, in both alloys, notably $\tau_{max}$ decreases with increasing temperature, indicating thermal activation due to the pinning of the loop to the dislocation line.

In the case of Y3-HEA, the highest pinning strength occurs when dislocations glide through the Frank loop at $I$=0.25, specifically targeting the lower half of the loop diameter, as depicted in Fig. 10b. This pinning strength weakens when dislocations glide just beneath the loop at $I$=0. However, it's noteworthy that dislocations can still be pinned even when they glide tangentially from the top or bottom of the loop due elastic strain around the dislocation, as observed at $I$=0 and $I$=1.

Remarkably, $\tau_{max}$ exhibits only slight differences at $I$=0.25, 0.5, and 0.75, as the Frank loop intersects with the gliding plane either at the top or bottom half of the loop, resulting in nearly identical obstacle strength. Additionally, all interaction mechanisms in these cases involve shearing. Similar trend was observed in ASS as shown in Fig. 10c.

Fig. 11 displays snapshots of a 10 *nm* Frank loop in Y3-HEA after detaching it from the dislocation line at 600 *K* and 900 *K*, highlighting different intersection interactions. In Fig 11a, the Frank loop at $I$=0.5 and 0.75, observed at 600 *K*, aligns the 1/3[111] dislocation segment with the [110] directions, leading to the formation of stair rod dislocations and additional faults within the inclined (111) plane. In contrast, at $I$=0.25 and 1, seen in Fig 11b at 900 *K*, the formation of a superjog is evident. These results emphasize that different intersection points of the mobile edge dislocation glide plane can lead to various reaction types. Most notably, it may also indicate that the possibilities of loop absorption and unfaulting increase with rising temperature, as depicted in Fig. 11b.

It is worth noting that this discussion primarily focuses on Frank loops. However, in reality, the presence of perfect loops interacting with mobile gliding dislocations can also play a significant role when various intersections occur. This aspect is evident in the work of Bakaev et al.

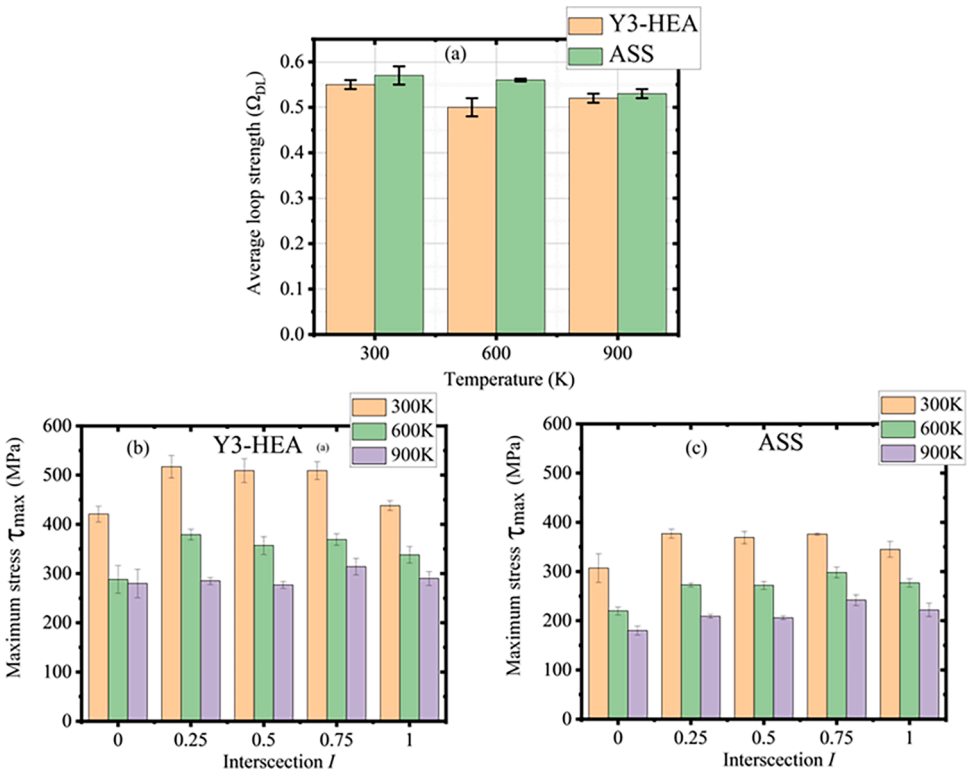


**Fig. 10.** Interaction strength between a glissile edge dislocation in (111) glide plane and 10 nm – (Franck loop): (a) bar plot of average obstacle strength with error bar as a function of temperature; the maximum stress as a function of different intersection height $I$ for different temperatures in (b) Y3-HEA and c) ASS. Reminder: $\tau_{max}$ is the maximum stress attained during unpinning of obstacle from the dislocation line.

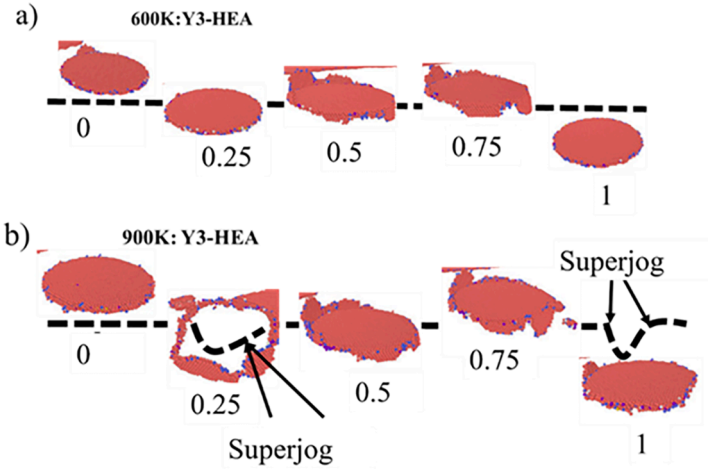


**Fig. 11.** Demonstration of intersection impact on interaction mechanisms. Loop reactions following unpinning from dislocation lines in Y3-HEA at 600 and 900 K for 10 nm Frank loop size. The black dotted lines indicate the dislocation gliding plane (111).

[54], which revealed that edge dislocations tend to absorb perfect loops more frequently than Frank loops, irrespectively of loop size. Additionally, it was demonstrated that perfect loops present a more complex obstacle for moving screw dislocations compared to edge dislocations. These aspects will be further investigated in the case of Y3-HEA.

#### 4.2.2. *Prediction of hardening induced by dislocation loop*

To practically apply Eq. (15) for predicting the impact of dislocation loop-induced hardening, we utilized an illustrative example resembling conditions within a nuclear reactor environment. This example involved a 10 *nm* loop size and a temperature of 600 *K*, and we based our calculations on atomistic simulation data.

The loop density ($N_{DL}$) in our simulation was estimated by calculating ($1/V$), where $V$ represents the volume of the simulation box as detailed in section 2.2. The shear modulus (μ) was determined using the Hill approximation and is provided in Table 1 for various temperatures in *GPa*.

In Fig. 12, we present an estimation of dislocation loop (DL) hardening for two alloy materials: austenitic stainless steel (ASS) and Y3-HEA, both featuring a loop diameter of 10 *nm*. Parameters from Table 8 have been used. The estimated $\tau_{DL}$ hardening values are 194 *MPa* for Y3-HEA and 202 *MPa* for ASS, showing only a slight difference between the two alloys. It's worth noting that the reliability of the estimation for ASS is supported by analytical estimations conducted by

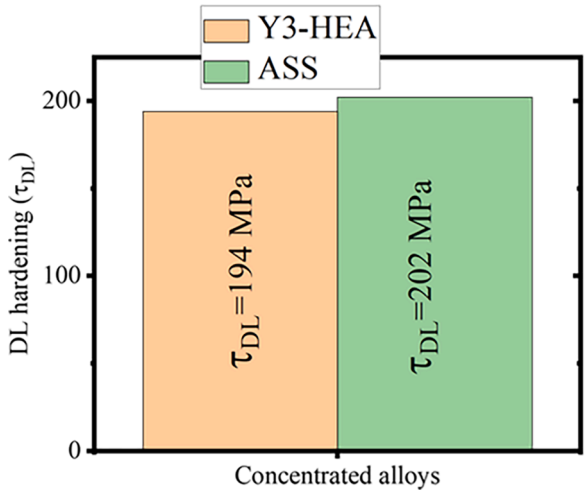


**Fig. 12.** Bar plot for dislocation loop (DL) hardening in Y3-HEA and ASS using Eq. (15) for 600 K with the data provided in Table 8.

**Table 8**
Parameters for constitutive Eq. (15) at 600 K.

| Material/ | Parameters | | | | | |
|---|---|---|---|---|---|---|
| | $\bar{\Omega}_{DL}$ | $\mu$ (GPa) | b (nm) | $N_{DL}$ ( $m^{-3}$) | $D_{DL}$(nm) | $\tau_{DL}$ (MPa) |
| ASS | 0.56 | 77 | 0.250 | $3.5 \times 10^{22}$ | 10 | 202 |
| Y3-HEA | 0.50 | 83 | 0.249 | | | 194 |

Monnet and Mai [50], which yielded a similar result of $\tau_{DL} = 192$ *MPa* despite differences in loop density.

However, it is crucial to emphasize that this study considered only the impact of dislocation loop (DL) hardening in radiation hardening on both alloys. For an accurate estimation of radiation hardening, it is necessary to account for the collective effects of all the microstructure defects, such as voids, dislocation networks, and precipitates that may present in the alloys as demonstrated by Monnet et al. [51].

In fact, as demonstrated by Monnet al. [50,51], the presence of a high density of other defects in an irradiated microstructure can diminish the hardening effect of dislocation loops.

The contribution of dislocation loops to radiation hardening in Y3-HEA is not yet fully understood experimentally. However, despite the minor difference in DL hardening contribution between Y3-HEA and ASS as depicted in Fig. 12, our investigation suggest that certain austenitic high-entropy alloys (HEAs) may exhibit lower radiation hardening than austenitic stainless steel (ASS) under similar irradiation conditions. Additional research is needed to investigate the influence of local chemical complexity on obstacle strength. This exploration may reveal whether a notable difference in dislocation loop hardening between Y3-HEA and ASS can be observed. While quantifying hardening at the atomistic level remains challenging, qualitative predictions based on the effect of chemical complexity on dislocation loops can inform the future design of HEAs for structural applications.

## 5. Conclusion

Atomistic simulations using molecular statics (MS) and molecular dynamics (MD) were conducted to explore the interaction between a Frank loop and a mobile edge dislocation in two materials: a model austenitic high-entropy alloy with the composition $Cr_{15}Fe_{46}Mn_{17}Ni_{22}$, referred to as Y3-HEA, and a model austenitic stainless steel (ASS) with the composition $Cr_{20}Fe_{70}Ni_{10}$. The results from the atomistic simulations were extrapolated to classical continuum theory, yielding the following conclusions:

I. The critical size for Frank loop unfaulting is slightly higher in Y3-HEA compared to ASS. At 0 *K*, the critical size was found to be 14 *nm* for Y3-HEA and 12 *nm* for ASS. These values align with existing literature, suggesting that Frank loops unfault into perfect loops above a critical size range of 8–12 *nm*.
II. Both materials exhibited three primary reaction mechanisms: loop absorption, loop unfaulting, and loop shearing. These mechanisms depend on factors such as temperature, loop size, orientation, and random seed configurations. In Y3-HEA with a 2 *nm* loop size, loop shearing dominated across all simulation conditions, while in ASS, loop unfaulting prevailed at high temperatures due to thermal activation. This discrepancy aligns with experimental findings, indicating that ASS requires a loop size of 12 *nm* at high irradiation temperatures for unfaulting to occur. The difference between the alloys can be attributed, in part, to significant fluctuations in local stacking fault energy (SFE) in Y3-HEA. However, at larger loop sizes of 5 *nm* and 10 *nm*, both alloys exhibited similar interaction mechanisms, with loop shearing being the predominant reaction in approximately 95% of cases.
III. In Y3-HEA at 900 *K* with a 2 *nm* loop, a novel interaction mechanism was observed, termed the "formation of a mobile superjog along the Shockley partial." This phenomenon involved the loop being positioned at $\delta$=1/3[111]. Following loop absorption, the superjog displayed mobility as it shifted along the trailing partial dislocation. This suggests the presence of a mobile superjog on the trailing partial dislocation, contributing to a reduction in overall hardening.
IV. Thermal activation influenced the probabilities of loop absorption and unfaulting reactions in both Y3-HEA and ASS. As temperature increased, the probability of these reactions also increased, leading to reduced hardening effects compared to shearing reactions.
V. The critical stress required to unpin mobile edge dislocations from the Frank loop during an interaction was analyzed. Estimates indicate that, under various simulation conditions, the critical stress in Y3-HEA exceeded that in the ASS alloy.
VI. An average obstacle strength parameter was calculated based on MD data and integrated into a radiation hardening model to predict the hardening caused by dislocation loops at different temperatures. At 600 *K*, Y3-HEA is slightly lower than dislocation loop hardening (194 *MPa*) compared to ASS (202 *MPa*). This suggests a potential decrease in radiation damage in austenitic high-entropy alloys when compared with traditional austenitic stainless steels. The calculated average obstacle strength parameter can be further utilized in higher-scale simulations, such as discrete dislocation dynamics.

## Data availability

All data included in this study are available upon request by contact with the corresponding author.

## Declaration of competing interest

The authors declare that they have no known competing financial interests or personal relationships that could have appeared to influence the work reported in this paper.

## Acknowledgments

Our research was funded by the French ANR-PRCE-HERIA project (ANR-19-CE08-0012-01). One of the authors (GB) received support from the Euratom research and training program 2019-2020 through the ENTENTE project, under grant agreement No. 900018.

## Supplementary materials

Supplementary material associated with this article can be found, in the online version, at doi:10.1016/j.jnucmat.2024.154959.

## References


[1] G.S. Was, Fundamentals of Radiation Materials Science, Springer Berlin Heidelberg, Berlin, Heidelberg, 2007.

[2] X. Li, A. Almazouzi, Deformation and microstructure of neutron irradiated stainless steels with different stacking fault energy, J. Nucl. Mater. 385 (2009) 329–333, https://doi.org/10.1016/j.jnucmat.2008.12.008.

[3] G. Monnet, New insights into radiation hardening in face-centered cubic alloys, Scr. Mater. 100 (2015) 24–27, https://doi.org/10.1016/j.scriptamat.2014.12.003.

[4] S.J. Zinkle, G.S. Was, Materials challenges in nuclear energy, Acta Mater. 61 (2013) 735–758, https://doi.org/10.1016/j.actamat.2012.11.004.

[5] S.J. Zinkle, L.L. Snead, Designing radiation resistance in materials for fusion energy, Annu. Rev. Mater. Res. 44 (2014) 241–267, https://doi.org/10.1146/annurev-matsci-070813-113627.

[6] B. Cantor, I.T.H. Chang, P. Knight, A.J.B. Vincent, Microstructural development in equiatomic multicomponent alloys, Mater. Sci. Eng. A 375–377 (2004) 213–218, https://doi.org/10.1016/j.msea.2003.10.257.

[7] B. Gludovatz, A. Hohenwarter, D. Catoor, E.H. Chang, E.P. George, R.O. Ritchie, A fracture-resistant high-entropy alloy for cryogenic applications, Science 345 (2014) 1153–1158, https://doi.org/10.1126/science.1254581 (1979).

[8] G. Laplanche, A. Kostka, O.M. Horst, G. Eggeler, E.P. George, Microstructure evolution and critical stress for twinning in the CrMnFeCoNi high-entropy alloy, Acta Mater. 118 (2016) 152–163, https://doi.org/10.1016/j.actamat.2016.07.038.

[9] Z. Wu, H. Bei, G.M. Pharr, E.P. George, Temperature dependence of the mechanical properties of equiatomic solid solution alloys with face-centered cubic crystal structures, Acta Mater. 81 (2014) 428–441, https://doi.org/10.1016/j.actamat.2014.08.026.

[10] K. Jin, C. Lu, L.M. Wang, J. Qu, W.J. Weber, Y. Zhang, H. Bei, Effects of compositional complexity on the ion-irradiation induced swelling and hardening in Ni-containing equiatomic alloys, Scr. Mater. 119 (2016) 65–70, https://doi.org/10.1016/j.scriptamat.2016.03.030.

[11] N.A.P.K. Kumar, C. Li, K.J. Leonard, H. Bei, S.J. Zinkle, Microstructural stability and mechanical behavior of FeNiMnCr high entropy alloy under ion irradiation, Acta Mater. 113 (2016) 230–244, https://doi.org/10.1016/j.actamat.2016.05.007.

[12] C. Parkin, M. Moorehead, M. Elbakhshwan, X. Zhang, P. Xiu, L. He, M. Bachhav, K. Sridharan, A. Couet, Phase stability, mechanical properties, and ion irradiation effects in face-centered cubic CrFeMnNi compositionally complex solid-solution alloys at high temperatures, J. Nucl. Mater. 565 (2022) 153733, https://doi.org/10.1016/j.jnucmat.2022.153733.

[13] J.J. Gao, B. Décamps, A. Fraczkiewicz, A.C. Bach, T. Jourdan, E. Meslin, Temperature effect on radiation-induced dislocation loops in a FCC high purity CrFeMnNi multi-principal element alloy, Materialia 26 (2022) 101580, https://doi.org/10.1016/j.mtla.2022.101580.

[14] Z. Wu, H. Bei, Microstructures and mechanical properties of compositionally complex Co-free FeNiMnCr18 FCC solid solution alloy, Mater. Sci. Eng. A 640 (2015) 217–224, https://doi.org/10.1016/j.msea.2015.05.097.

[15] C. Li, X. Hu, T. Yang, N.K. Kumar, B.D. Wirth, S.J. Zinkle, Neutron irradiation response of a Co-free high entropy alloy, J. Nucl. Mater. 527 (2019) 151838, https://doi.org/10.1016/j.jnucmat.2019.151838.

[16] J. Olszewska, Conception and Development of a Novel Grade of High Resistance High Entropy Alloy from the CrFeMnNi family, Ecole des MINES Saint Etienne, 2019. PhD Thesis.

[17] D. Chen, K. Murakami, K. Dohi, K. Nishida, Z. Li, N. Sekimura, The effects of loop size on the unfaulting of Frank loops in heavy ion irradiation, J. Nucl. Mater. 529 (2020) 151942, https://doi.org/10.1016/j.jnucmat.2019.151942.

[18] C. Chen, J. Zhang, J. Song, Comprehensive study of vacancy frank loop unfaulting: atomistic simulations and predictive model, Acta Mater. 208 (2021) 116745, https://doi.org/10.1016/j.actamat.2021.116745.

[19] T. Kadoyoshi, H. Kaburaki, F. Shimizu, H. Kimizuka, S. Jitsukawa, J. Li, Molecular dynamics study on the formation of stacking fault tetrahedra and unfaulting of Frank loops in fcc metals, Acta Mater. 55 (2007) 3073–3080, https://doi.org/10.1016/j.actamat.2007.01.010.

[20] J.B. Baudouin, A. Nomoto, M. Perez, G. Monnet, C. Domain, Molecular dynamics investigation of the interaction of an edge dislocation with Frank loops in Fe–Ni10–Cr20 alloy, J. Nucl. Mater. 465 (2015) 301–310, https://doi.org/10.1016/j.jnucmat.2015.05.030.

[21] D. Terentyev, A. Bakaev, Interaction of a screw dislocation with Frank loops in Fe–10Ni–20Cr alloy, J. Nucl. Mater. 442 (2013) 208–217, https://doi.org/10.1016/j.jnucmat.2013.08.044.

[22] T. Nogaret, C. Robertson, D. Rodney, Atomic-scale plasticity in the presence of Frank loops, Philos. Mag. 87 (2007) 945–966, https://doi.org/10.1080/14786430601011497.

[23] D. Rodney, Molecular dynamics simulation of screw dislocations interacting with interstitial frank loops in a model FCC crystal, Acta Mater. 52 (2004) 607–614, https://doi.org/10.1016/j.actamat.2003.09.044.

[24] D. Rodney, G. Martin, Dislocation pinning by glissile interstitial loops in a nickel crystal: a molecular-dynamics study, Phys. Rev. B 61 (2000) 8714–8725, https://doi.org/10.1103/PhysRevB.61.8714.

[25] D. Rodney, G. Martin, Dislocation pinning by small interstitial loops: a molecular dynamics study, Phys. Rev. Lett. 82 (1999) 3272–3275, https://doi.org/10.1103/PhysRevLett.82.3272.

[26] A. Daramola, G. Bonny, G. Adjanor, C. Domain, G. Monnet, A. Fraczkiewicz, Development of a plasticity-oriented interatomic potential for CrFeMnNi high entropy alloys, Comput. Mater. Sci. 203 (2022) 111165, https://doi.org/10.1016/j.commatsci.2021.111165.

[27] G. Bonny, N. Castin, D. Terentyev, Interatomic potential for studying ageing under irradiation in stainless steels: the FeNiCr model alloy, Model. Simul. Mater. Sci. Eng. 21 (2013) 085004, https://doi.org/10.1088/0965-0393/21/8/085004.

[28] G. Bonny, D. Terentyev, R.C. Pasianot, S. Poncé, A. Bakaev, Interatomic potential to study plasticity in stainless steels: the FeNiCr model alloy, Model. Simul. Mater Sci. Eng. 19 (2011) 085008, https://doi.org/10.1088/0965-0393/19/8/085008.

[29] A. Daramola, A. Fraczkiewicz, G. Bonny, A. Nomoto, G. Adjanor, C. Domain, G. Monnet, Atomistic investigation of elementary dislocation properties influencing mechanical behaviour of Cr15Fe46Mn17Ni22 alloy and Cr20Fe70Ni10 alloy, Comput. Mater. Sci. 211 (2022) 111508, https://doi.org/10.1016/j.commatsci.2022.111508.

[30] Y.N. Osetsky, D.J. Bacon, An atomic-level model for studying the dynamics of edge dislocations in metals, Model. Simul. Mater. Sci. Eng. 11 (2003) 427–446, https://doi.org/10.1088/0965-0393/11/4/302.

[31] N. Grønbech-Jensen, N.R. Hayre, O. Farago, Application of the G-JF discrete-time thermostat for fast and accurate molecular simulations, Comput. Phys. Commun. 185 (2014) 524–527, https://doi.org/10.1016/j.cpc.2013.10.006.

[32] S. Plimpton, Fast parallel algorithms for short-range molecular dynamics, J. Comput. Phys. 117 (1995) 1–19, https://doi.org/10.1006/jcph.1995.1039.

[33] A. Stukowski, Structure identification methods for atomistic simulations of crystalline materials, Model. Simul. Mater. Sci. Eng. 20 (2012) 045021, https://doi.org/10.1088/0965-0393/20/4/045021.

[34] A. Stukowski, Visualization and analysis of atomistic simulation data with OVITO–the open visualization tool, Model. Simul. Mater. Sci. Eng. 18 (2010) 015012, https://doi.org/10.1088/0965-0393/18/1/015012.

[35] C. Varvenne, O. Mackain, E. Clouet, Vacancy clustering in zirconium: an atomic-scale study, Acta Mater. 78 (2014) 65–77, https://doi.org/10.1016/j.actamat.2014.06.012.

[36] S. Hayakawa, T. Okita, M. Itakura, T. Kawabata, K. Suzuki, Atomistic simulations for the effects of stacking fault energy on defect formations by displacement cascades in FCC metals under Poisson's deformation, J. Mater. Sci. 54 (2019) 11096–11110, https://doi.org/10.1007/s10853-019-03688-1.

[37] K. Dang, L. Capolungo, D.E. Spearot, Nanoscale dislocation shear loops at static equilibrium and finite temperature, Model. Simul. Mater. Sci. Eng. 25 (2017) 085014, https://doi.org/10.1088/1361-651X/aa9390.

[38] M. Desormeaux, B. Rouxel, A.T. Motta, M. Kirk, C. Bisor, Y. de Carlan, A. Legris, Development of radiation damage during in-situ Kr++ irradiation of Fe Ni Cr model austenitic steels, J. Nucl. Mater. 475 (2016) 156–167, https://doi.org/10.1016/j.jnucmat.2016.04.012.

[39] P. Xiu, H. Bei, Y. Zhang, L. Wang, K.G. Field, STEM characterization of dislocation loops in irradiated FCC alloys, J. Nucl. Mater. 544 (2021) 152658, https://doi.org/10.1016/j.jnucmat.2020.152658.

[40] C. Dai, Q. Wang, P. Saidi, B. Langelier, C.D. Judge, M.R. Daymond, M.A. Mattucci, Atomistic structure and thermal stability of dislocation loops, stacking fault tetrahedra, and voids in face-centered cubic Fe, J. Nucl. Mater. 563 (2022) 153636, https://doi.org/10.1016/j.jnucmat.2022.153636.

[41] B. Christiaen, C. Domain, L. Thuinet, A. Ambard, A. Legris, A new scenario for ⟨c⟩ vacancy loop formation in zirconium based on atomic-scale modeling, Acta Mater. 179 (2019) 93–106, https://doi.org/10.1016/j.actamat.2019.07.030.

[42] D.B. Miracle, O.N. Senkov, A critical review of high entropy alloys and related concepts, Acta Mater. 122 (2017) 448–511, https://doi.org/10.1016/j.actamat.2016.08.081.

[43] S. Hayakawa, Y. Hayashi, T. Okita, M. Itakura, K. Suzuki, Y. Kuriyama, Effects of stacking fault energies on the interaction between an edge dislocation and an 8.0-nm-diameter Frank loop of self-interstitial atoms, Nucl. Mater. Energy 9 (2016) 581–586, https://doi.org/10.1016/j.nme.2016.10.010.

[44] S.J. Zinkle, P.J. Maziasz, R.E. Stoller, Dose dependence of the microstructural evolution in neutron-irradiated austenitic stainless steel, J. Nucl. Mater. 206 (1993) 266–286, https://doi.org/10.1016/0022-3115(93)90128-L.

[45] D.H. Hull, D.J. Bacon, Introduction to Dislocations, Butterworth-Heineman, Oxford, 2011.

[46] M. Suzuki, A. Sato, T. Mori, J. Nagakawa, N. Yamamoto, H. Shiraishi, *In situ* deformation and unfaulting of interstitial loops in proton-irradiated steels, Philos. Mag. A 65 (1992) 1309–1326, https://doi.org/10.1080/01418619208205606.

[47] D.S. Gelles, A frank loop unfaulting mechanism in FCC metals during neutron irradiation. In: Dislocation Modelling of Physical Systems, Elsevier, 1981, pp. 158–162.

[48] D. Terentyev, A. Bakaev, Y.N. Osetsky, Interaction of dislocations with Frank loops in Fe–Ni alloys and pure Ni: An MD study, J. Nucl. Mater. 442 (2013) S628–S632, https://doi.org/10.1016/j.jnucmat.2013.01.328.

[49] C. Lu, T. Yang, K. Jin, N. Gao, P. Xiu, Y. Zhang, F. Gao, H. Bei, W.J. Weber, K. Sun, Y. Dong, L. Wang, Radiation-induced segregation on defect clusters in single-phase concentrated solid-solution alloys, Acta Mater. 127 (2017) 98–107, https://doi.org/10.1016/j.actamat.2017.01.019.

[50] G. Monnet, C. Mai, Prediction of irradiation hardening in austenitic stainless steels: analytical and crystal plasticity studies, J. Nucl. Mater. 518 (2019) 316–325, https://doi.org/10.1016/j.jnucmat.2019.03.001.

[51] G. Monnet, Multiscale modeling of irradiation hardening: application to important nuclear materials, J. Nucl. Mater. 508 (2018) 609–627, https://doi.org/10.1016/j.jnucmat.2018.06.020.
[52] L. Tan, J.T. Busby, Formulating the strength factor α for improved predictability of radiation hardening, J. Nucl. Mater. 465 (2015) 724–730, https://doi.org/10.1016/j.jnucmat.2015.07.009.
[53] G. Monnet, B. Devincre, Solute friction and forest interaction, Philos. Mag. 86 (2006) 1555–1565, https://doi.org/10.1080/14786430500398425.
[54] A.V. Bakaev, D.A. Terentyev, P.Yu. Grigor'ev, E.E. Zhurkin, Interaction between mobile dislocations and perfect dislocation loops in Fe-Ni-Cr austenitic alloy systems, J. Surf. Investig. 9 (2015) 290–299, https://doi.org/10.1134/S1027451015020056. X-ray, Synchrotron and Neutron Techniques.